Physics of Fluids

Spatial distribution of the quantized vortices' tangle in thermally driven round jets of superfluid helium

Cite as: Phys. Fluids **35**, 035136 (2023); https://doi.org/10.1063/5.0145058
Submitted: 02 February 2023 • Accepted: 08 March 2023 • Published Online: 22 March 2023

P. Švančara, P.-E. Roche and M. La Mantia

AIP Publishing

Physics of Fluids ARTICLE scitation.org/journal/phf

Spatial distribution of the quantized vortices' tangle in thermally driven round jets of superfluid helium

Cite as: Phys. Fluids **35**, 035136 (2023); doi: 10.1063/5.0145058
Submitted: 2 February 2023 · Accepted: 8 March 2023 ·
Published Online: 22 March 2023

View Online Export Citation CrossMark

P. Švančara,[1,a] P.-E. Roche,[2] and M. La Mantia[1]

AFFILIATIONS

[1]Faculty of Mathematics and Physics, Charles University, Ke Karlovu 3, 121 16 Prague, Czech Republic
[2]Institut Néel, CNRS-UGA, 25 Avenue des Martyrs, 38042 Grenoble Cedex 9, France

[a]**Present address:** School of Mathematical Sciences, University of Nottingham, University Park, NG7 2RD Nottingham, United Kingdom. **Author to whom correspondence should be addressed:** patrik.svancara@nottingham.ac.uk

ABSTRACT

Thermally driven flows of superfluid ^{4}He display unique features, often related to the presence of quantized vortices—line singularities embedded in the liquid. Here, we focus on turbulent round jets, experimentally investigated using the flow visualization and second sound attenuation techniques, at Reynolds numbers exceeding 10^4. These turbulent flows are driven by releasing heat into a small volume of liquid, open to the surrounding bath through a cylindrical nozzle, 2 mm in diameter. Our measurements reveal in unprecedented detail how the tangle of quantized vortices associated with the jets arranges itself in space, for distances ranging from 9 to 34 nozzle diameters, at fluid temperatures between 1.64 and 2.10 K. We specifically find that the vortex tangle spreads in the radial direction, while it dilutes away from the nozzle. Additionally, the tangle density is found to systematically depend on the flow forcing. Two physical interpretations of the observed behavior are proposed, which could motivate further investigations of this peculiar flow. One leads us to conjecture a self-similar functional form of the vortex tangle density across counterflow jets. The other suggests that the position of the superfluid stagnation point—a characteristic feature of counterflow jets—could depend on the flow forcing as well.

I. INTRODUCTION

Turbulent jets are typical representatives of boundary-free shear flows that can be realized not only in classical Newtonian fluids but also in superfluid ^{4}He, e.g., see Refs. 1 and 2. A jet flow is usually obtained by driving a fluid stream through a nozzle into a large reservoir. The interaction between the injection flow, the nozzle, and the fluid inside the reservoir results in a distinct, spatially inhomogeneous structure that can be experimentally studied. In the present work, we focus on turbulent round jets submerged in superfluid ^{4}He, also known as He II. This phase of liquid ^{4}He exists only at temperatures below approximately 2.2 K, at the saturated vapor pressure, and its behavior is appreciably affected by the quantum order that spontaneously develops in the fluid. Macroscopic consequences of this order are, for example, the possible occurrence of inviscid flows and the coupling between temperature and pressure gradients (the fountain effect)—see Refs. 3 and 4 for reviews on this unique liquid.

At temperatures higher than about 1 K, thermal excitations cannot be neglected and the large-scale hydrodynamics of He II is usually described by the phenomenological two-fluid model.[5,6] The gas of excitations can be seen as a viscous fluid called the normal component, while the quantum-ordered system behaves as an inviscid, superfluid component. The two fluid components are fully miscible, and their density fractions, which depend only on temperature, are plotted in Fig. 1 for the range of temperatures relevant here—note in passing that the He II density $\rho \approx 145$ kg/m^3 depends weakly on temperature.[7]

Additionally, the circulation of the superfluid component is quantized.[8] Specifically, each circulation quantum $\kappa \approx 10^{-7}$ m^2/s is associated with a quantized vortex, which is a line singularity of the quantum order parameter characterized by a narrow core (approximately 0.1 nm) and macroscopic length. When superfluid ^{4}He becomes turbulent, quantized vortices tend to interact and eventually form a dynamic tangle, which is the key component of turbulence in He II.[3,4] Here, we employ experimental tools to study the quantized vortices' tangle associated with steady turbulent jets, in view of understanding in what aspects jet flows in superfluid ^{4}He may differ from their classical analogs. The quantized vortices' tangle plays an

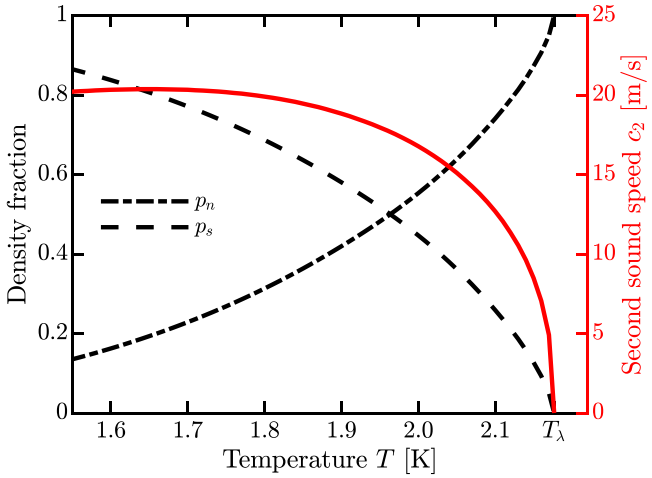

FIG. 1. Left axis: temperature dependence of the density fractions of the normal (p_n, dot-dashed line) and superfluid (p_s, dashed line) components of He II. Right axis: temperature dependence of the second sound speed (solid line). $T_\lambda \approx 2.2$ K denotes the superfluid transition at the saturated vapor pressure. Data from Ref. 7.

important role in this context because it provides the coupling mechanism between the otherwise independent components of He II. At flow scales larger than the mean distance ℓ between quantized vortices, the magnitude of this interaction—usually called mutual friction force—is proportional to the difference between the velocities of the normal (v_n) and superfluid (v_s) components.[3,4]

According to the just outlined model, when heat is dissipated in He II, two velocity fields pointing in opposite directions are established, resulting in the so-called thermal counterflow. The normal component flows away from the heat source, dispersing heat into the ^{4}He bath, while the superfluid component, which has zero entropy and therefore cannot transport heat, flows in the opposite direction, to compensate for the mass flow of the normal component. In the widely studied case of channel counterflow, a heating power P is dissipated at the closed end of a channel with cross section S, submerged in a liquid bath kept at temperature T. In the steady state, the normal component moves toward the open end of the channel with the average velocity

$$v_n = \frac{q}{\rho s T}, \tag{1}$$

where $q = P/S$ is the dissipated heat flux, ρ indicates the density of He II, and s is the fluid specific entropy. In order to satisfy the null mass flow rate condition just mentioned, the superfluid component flows toward the heater with the average velocity v_s in such a way that $p_n v_n = -p_s v_s$ holds (we assume here that $v_n > 0$ and $v_s < 0$). As a result, the relative velocity of the two components is in general nonzero. We usually denote this velocity difference as the counterflow velocity v_{ns}, which is then given as

$$v_{ns} = v_n - v_s = \frac{q}{\rho_s s T} = \frac{v_n}{1 - p_n}, \tag{2}$$

where $\rho_s = p_s \rho$ is the density of the superfluid component.

Here, we take advantage of the just outlined flow regime because our turbulent jets are driven thermally, by dissipating a constant heating power in a small enclosed volume open to the He II bath via a cylindrical nozzle. The resulting flow is usually named thermal counterflow jet—see Ref. 9 for a review on early works—and in the past, it was mainly regarded as a playground system for the study of the mutual friction force in the absence of solid boundaries, which significantly influence the development of turbulence in He II, as recently discussed in Refs. 10–13.

Following Ref. 14, we define a Reynolds number relevant for thermal counterflow jets as

$$\mathrm{Re} = \frac{\rho v_n d}{\mu_n}, \tag{3}$$

where d indicates the nozzle diameter, and μ_n denotes the dynamic viscosity of He II. As detailed below, the Re values achieved in the present work are larger than the critical value of 5×10^3 reported in Ref. 14, on the basis of flow visualization experiments. It then follows that our thermally driven jets are turbulent. Additionally, one expects that the mutual friction force is significantly enhanced in the nozzle output region because a dense tangle of quantized vortices develops within the nozzle itself, partly due to the interaction of the flow with the inner wall of the nozzle, and partly due to the mutual interaction between the normal and superfluid components.[11] Consequently, the fast-moving normal component exits the nozzle and interacts with the vortices, which are flushed into the open volume, where their presence can be probed in various ways, e.g., by negative ion trapping.[15]

Thermometric measurements carried out along the jet axis—e.g., see Refs. 16 and 17—reveal that a temperature difference ΔT develops inside the nozzle, i.e., the fluid temperature in the bath is smaller than that inside the nozzle. For example, the $\Delta T \propto q^3$ scaling obtained at heat fluxes higher than about 5 kW/m^2—and typical of turbulent counterflow in channels[18]—confirms that a dense tangle of quantized vortices should be present inside the nozzle in these conditions. However, the temperature gradient seems to disappear about one diameter away from the nozzle, as reported, e.g., in Ref. 16, at least for relatively high heat flux values, i.e., within the just mentioned cubic regime. On the basis of this evidence, it was conjectured that the superfluid component might be coupled to the normal one in the free jet flow, resulting then in a nearly zero counterflow velocity (i.e., coflow of the normal and superfluid components) in the far field. The hypothesis was later supported by acoustic attenuation,[19] velocity-sensitive phase,[20] and laser Doppler velocimetry measurements, as close as $0.5d$ above the nozzle.[21,22] Additionally, it was found that the fluid velocity at the nozzle exit is apparently equal to $p_n v_n$, which can be explained by the transfer of momentum between the normal component, which exits the nozzle with a velocity v_n, and the surrounding superfluid one, via a process similar to the turbulent entrainment known to occur for classical turbulent jets.[9,23] It then follows that the flow field of the superfluid component must have a stagnation point near the nozzle.[9,22] We schematically sketch this velocity field in Fig. 2.

Additionally, following Ref. 24, one can split the flow field of turbulent jets into three regions. The near field region, extending up to seven nozzle diameters away from the nozzle, can be considered as the region of flow establishment. Then, some self-similar properties of turbulent jets are expected to emerge in the intermediate field region, and the flow is said to be fully developed only in the far field region, corresponding to more than 70 nozzle diameters away from the nozzle. Here, we focus on the intermediate field region of free counterflow

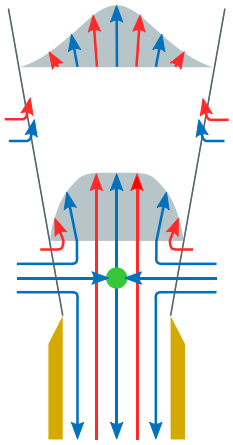

FIG. 2. Sketch of the two-component flow field in a thermal counterflow jet. Red (blue) arrows: normal (superfluid) component; green point: stagnation point of the superfluid component. Displayed are also velocity profiles in the near field, i.e., in the close proximity of the nozzle (bottom) and in the intermediate field (top), see Eq. (4). Adapted from Ref. 22.

jets, where the resulting single-component flow field of He II already resembles to some extent the Newtonian one, as shown, for example, in Ref. 25. Specifically, it was reported that the radial profile of the flow velocity is nearly Gaussian[24,25] and that the profile width grows linearly with axial distance, the latter being associated with the similarity of the flow field.[26,27] The vertical component of the fluid velocity can then be written as

$$v(r,z) = v_0(z)\exp\left[-\left(\frac{r}{\beta z}\right)^2\right] \tag{4}$$

in the cylindrical coordinates (r, ϕ, z), where v_0 is the centerline velocity, along the jet axis, and β indicates the jet growth rate. The centerline velocity was found to be constant for the first one to four nozzle diameters away from the nozzle,[25] and, for larger distances, the classical $v_0 \propto z^{-1}$ scaling holds.[26,27] Note also that in Ref. 22 the flow development region of counterflow jets was reported to be somehow shorter than that of ordinary turbulent jets.

On the other hand, there is little known about the spatial structure of the quantized vortices' tangle in a thermal counterflow jet. In this work, we aim to fill in this knowledge gap and we present the first spatially resolved measurements of the vortex line density $L(r, z)$ in this kind of flow, where L is defined as the total length of quantized vortices per unit volume. We specifically probe the quantized vortices' tangle using the second sound attenuation technique.[6,28,29] The latter is based on detecting temperature waves, which can be observed in flows of superfluid ^{4}He. Within the two-fluid framework, the second sound waves consist of anti-phase oscillations of the normal and superfluid components, while the well-known density (pressure) waves—named first sound waves in He II—correspond instead to in-phase oscillations of the components. The speed of the second sound is temperature dependent—it reaches a flat maximum near 1.65 K and steeply decreases near the superfluid transition temperature, as shown in Fig. 1 (right axis).

In summary, as detailed below, we find that the quantized vortices' tangle spreads in the radial direction, along the jet axis, in a way similar to that observed for the fluid velocity, while its peak density decreases away from the flow source. We then discuss, on the basis of several assumptions, the spatial distribution and the flow forcing dependence of the tangle density, directly obtained from the experimental data.

II. METHODS

The counterflow jets here investigated are obtained at the bottom of a standard ^{4}He cryostat by supplying constant heating power to a resistive heater located inside a purpose-made enclosure, 3D-printed from copper filled PLA—see Ref. 30 for a detailed description of the apparatus and for preliminary results that are further discussed in the following. The enclosure is terminated by a circular nozzle, with the inner diameter $d = 2$ mm, as sketched in Fig. 3—the nozzle is machined from brass and is $5d$ high. The thermally driven jets develop in the open volume above the nozzle—the diameter of this volume is approximately $75d$, and it is at least $350d$ high.

The vortex line density embedded in the flow is measured with a miniature second sound sensor[29,31,32] consisting of two silicon plates placed $\delta = (2.505 \pm 0.002)$ mm apart. The plates support a heater-thermometer pair, microfabricated at their respective extremities. The sensor's cross section in the direction of the flow at the measurement location is approximately twice 1 mm × 20 μm, and about 14 mm downstream this measurement location, the sensor's cross section enlarges to approximately 2.5 × 3.5 mm^2. The heater is supplied with a sine-wave voltage signal with frequency f, and, in consequence, second sound waves with frequency $2f$ are emitted toward the thermometer, which in turn develops weak periodic oscillations of its resistance. To

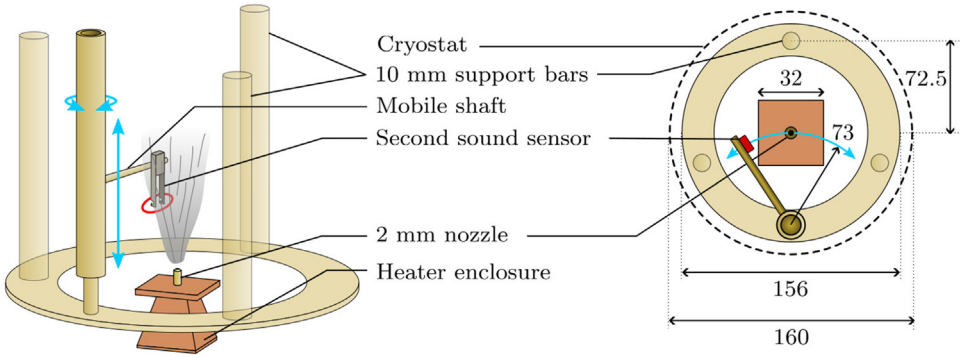

FIG. 3. Sketch of the experimental setup (not to scale). Brown: 3D-printed heater enclosure; blue arrows: possible motions of the mobile shaft; red: sensitive area of the second sound sensor. Dimensions in the right panel are in millimeters.

readout this signal, the thermometer is supplied with a small constant current and we collect the corresponding voltage oscillations by a lock-in amplifier.

The two plates of the sensor form an open resonance cavity, and standing second sound waves are obtained between them when the driving frequency f equals the resonance frequency f_n, which can be approximated as

$$f_n = \frac{nc_2}{4\delta}, \tag{5}$$

where n is a positive integer, and c_2 indicates the second sound speed, whose temperature dependence is plotted in Fig. 1 (right axis). By driving the device across resonance in quiescent He II, i.e., when the vortex line density is relatively small, we obtain a nearly Lorentzian resonance curve typical of harmonic oscillators, with amplitude A_0 and half-width Δ_0. In case the sensor is placed in a flow of He II containing a substantial vortex tangle, the second sound waves are attenuated by the action of the mutual friction force and the measured resonance amplitude A falls behind A_0. The ratio $A_0/A > 1$ can then be related to the vortex line density L. For a homogeneous and isotropic tangle, the latter can be approximately estimated[28,29] as

$$L = \frac{6\pi\Delta_0}{B\kappa}\left(\frac{A_0}{A} - 1\right), \tag{6}$$

where B denotes the mutual friction parameter, tabulated in Ref. 7. For a polarized (preferentially oriented) tangle, Eq. (6) is modified by a constant prefactor,[28] i.e., the relation can be used as a qualitative estimate of L also for polarized tangles, assuming that the polarization does not significantly change over the course of the experiment. Additionally, in Ref. 28, the uncertainty associated with Eq. (6) is reported to be of the order of 10%. Still, we find its use in this study adequate, because such a level of uncertainty is comparable to the statistical uncertainty of A and to other systematic errors specific to the employed sensor, which are discussed below.

Note also that the sensitivity of the second sound attenuation technique is further limited by the fact that it is based on the relative measurement of the two second sound amplitudes. In practice, solely amplitudes meeting $A/A_0 \lesssim 0.99$ can be distinguished. For the typical value $\Delta_0 = 300$ Hz, we estimate from Eq. (6) that at 1.95 K, the minimum density that can be faithfully detected is $L_{\min} \approx 6 \times 10^8$ m^{-2}. The latter corresponds to approximately 1.5 m of vortex lines localized between the heater-thermometer pair, i.e., to a mean distance ℓ between quantized vortices of approximately 40 μm—the volume where L is measured is equal to approximately 2.5 mm^3.

The crucial feature of our sensor is its ability to be displaced within the experimental volume, thanks to a mobile shaft (see Fig. 3), without significantly altering the flow, due to its relatively small size and cross section along the axial direction. Two room-temperature stepper motors control the shaft motion: One motor moves the shaft in the vertical direction, and the other rotates it about its axis. In the latter case, the sensor moves inside the cryostat along a circle intentionally crossing the vertical axis of the setup. The angular deflection of the shaft α can then be used to obtain the radial coordinate r relative to the jet axis as

$$r = 2R\sin\left(\frac{\alpha - \alpha_0}{2}\right), \tag{7}$$

where $R = 73$ mm $= 36.5d$ is the length of the horizontal mounting arm (see Fig. 3), and $\alpha_0 = 1.9^\circ \pm 0.3^\circ$ denotes the offset between the zero position of the sensor, manually set before the experimental campaign, and its actual value, determined from the acquired second sound signal (see Fig. 4)—this radial coordinate is signed because the sensor is allowed to move on both sides of the jet axis, i.e., negative values of r simply denote that the corresponding deflection angle $\alpha < \alpha_0$ (and vice versa). Additionally, the sensor is mounted asymmetrically on the horizontal arm, and the sensitive areas are located approximately $7d$ away from the support (see Fig. 3). As we show below, no significant differences in the acquired second sound signal are observed between the strokes on opposite sides of the jet's axis, which leads us to believe that possible blockage effects caused by the asymmetry in the mounting are negligible. Note also that possible blockage effects caused by the symmetrical body of the sensor have presumably the same strength, since both parts have comparable sizes and positions in the flow, i.e., possible blockage effects from the sensor body are expected to be negligible too. Finally, the vertical position z of the sensor, relative to the top of the nozzle, is obtained directly from the corresponding stepper motor, and it can be determined with the accuracy of approximately 1 mm.

To the best of our knowledge, we report here the first use of a mobile second sound sensor to probe a spatially inhomogeneous tangle of quantized vortices. So far, inhomogeneous tangles were investigated by several static sensors placed along a counterflow channel—see Ref. 28 for a few examples—or by multiple sensors located in different loci of the experimental setup, as e.g., in Ref. 32.

Before proceeding, we now mention two effects that might potentially bias the second sound measurements. First, in regions far away from the jet axis, the mean flow encounters the two plates of our sensor at nonzero angles of attack. The mean flow velocity at the location of the sensor, which can be up to approximately 0.1 m/s, as shown e.g., in Fig. 5, is significantly smaller than the velocities of the first and second sound waves—in the investigated temperature range these velocities reach their minima at 2.10 K and are equal to 222 and 13 m/s, respectively.[7] Thus, no significant supersonic effects are expected to occur when the mean flow changes its direction due to the sensor. Nevertheless, a velocity boundary layer is expected to develop along each plate,[11,33] and quantum vortices localized within these layers may contribute to additional attenuation of the measured signal. Specifically, boundary layer effects were investigated in turbulent flows of He II for similar sensors, at zero mean angle of attack.[29,31] Their contribution was found to be negligible, partly due to the small thickness of the sensor plates, and partly due to the fact that the velocity boundary layer is expected to be small compared to δ (see Ref. 29 for a more detailed discussion of this effect). Additionally, in comparison with Ref. 32, the effect of the boundary layer on the measured signal might be larger, due to the nonzero angles of attack, but, at the same time, the distance between our sensor plates δ is 2.5 times larger than that in the just cited paper, where $\delta \approx 1$ mm. In consequence, the contribution of boundary layers to the total signal attenuation is, in our case, reduced by a factor of roughly 2.5, at the cost of a lower spatial resolution.

The second source of bias is due to the advection of the second sound waves from the resonance cavity, which also accounts for increased signal attenuation. This advection effect is present in all types of the second sound resonators to a greater or lesser degree.[29] Specifically, the attenuation attributed to the vortex tangle is more significant, and Eq. (6) represents an accurate estimate of L when the

second sound sensor is operated with a low-order resonant mode. In our case, as detailed below, we use the 18th harmonic mode, which means that the second sound beam is more focused and sensitive to advection by the mean flow than it would be for lower order modes. From the comparison with other available sensor geometries, we estimate this bias to be as large as a few tens of percent (a more detailed discussion of this effect is reported in Ref. 29). It is, therefore, more significant than the other bias mentioned above, and, consequently, the additional sensitivity of the employed second sound sensor to the mean flow velocity should be kept in mind.

Aware of these drawbacks, we consolidate our second sound measurements using cryogenic flow visualization. The technique—discussed at length in Ref. 30—is based on following the flow-induced motions of micrometer-sized particles by a digital camera. We specifically visualize solid deuterium particles, which are illuminated by a 1 mm thick and 10 mm high laser sheet crossing the vertical axis of the jet. The acquired camera images are then processed to obtain particle trajectories and velocities. These measurements are carried out in an optical cryostat, with a 12 mm ($6d$) wide and 8 mm ($4d$) high field of view located approximately 10 mm ($5d$) above the nozzle, along the jet axis—see again Ref. 30 for experimental details.

III. EXPERIMENTAL RESULTS

Steady counterflow jets are investigated at three temperatures (approximately 1.65, 1.95, and 2.10 K) corresponding to normal component density fractions p_n of 0.19, 0.48, and 0.74, respectively. Note that the helium bath was kept at constant temperature by maintaining the associated helium vapors at constant pressure, i.e., the temperature standard deviation was less than 12 mK at 1.65 K, and around 1 mK at higher temperatures. Depending on the employed experimental protocol, we split the acquired datasets into four categories, labeled A, B, C, and D—see Table I for relevant experimental conditions.

Datasets A1–A3 were collected near 1.65 K because the temperature dependence of the second sound speed has a plateau here, see Fig. 1 (right axis). The resonance condition given by Eq. (5) then becomes insensitive to small temperature fluctuations experienced in almost every cryogenic setup. Therefore, we continuously excite the sensor at the fixed frequency $f = 37.22$ kHz, which corresponds to the 18th harmonic mode. By displacing the sensor, we sweep the volume above the nozzle and we then collect the second sound amplitude A for a set of positions given by (α, z). In order to increase the signal-to-noise ratio, multiple (at least 30) sweeps across the jet axis are performed for constant z and the resulting second sound amplitude is calculated as their average. The vortex-free resonance amplitude A_0 and the peak width Δ_0 are obtained by fitting the full resonance curves, purposely acquired far away from the jet axis, i.e., far away from the tangle.

An example of the acquired second sound signals is presented in the top panel of Fig. 4. Here, we show two sets of sweeps obtained near the extremities of the accessed axial distance, which are $9.0d$ and $31.5d$, respectively. Individual sweeps across the jet axis (points) as well as their ensemble averages (black lines) show a coherent response, with most of the attenuation taking place in a narrow region of sensor's angular deflections. Because this attenuation can be related to the presence of a quantized vortices' tangle, we use the obtained data to calculate the corresponding vortex line density and probe its spatial structure. Additionally, as shown in the bottom panel of Fig. 4, the fluctuations of the second sound amplitude introduce a statistical uncertainty of around 10%, which is comparable to the uncertainty one can associate with Eq. (6), as mentioned above—a similar level of fluctuations is observed for other axial distances and datasets A1–A2. Finally, no systematic error is apparently introduced by the stepper motor that displaces the sensor back and forth across the signal minimum, thanks to its positioning accuracy.

An approach similar to that used above is not possible for datasets in categories B and C because, for the corresponding temperatures, c_2 is strongly temperature dependent. Therefore, for each sensor position, a full frequency sweep across the resonance frequency (approximately 38.5 kHz) is measured and we estimate the corresponding resonance amplitude from the in-phase (A_x) and quadrature (A_y) components of the acquired signal,[28,29] since the plot of A_y as a function of A_x can be fitted with a circle having diameter equal to A. As in the previous case, the values of A_0 and Δ_0 are taken from full fits of the resonance curves measured far away from the jet. Following this approach, we obtain a single value of A for each position of the second sound sensor and the statistical fluctuations of the sensor response are, therefore, not available for these datasets.

While sets B1–B4 probe the jet in both radial and axial directions and can then be directly compared to A1–A3, the set C1 only captures the vortex line density along the jet axis, i.e., for a constant angular deflection equal to α_0.

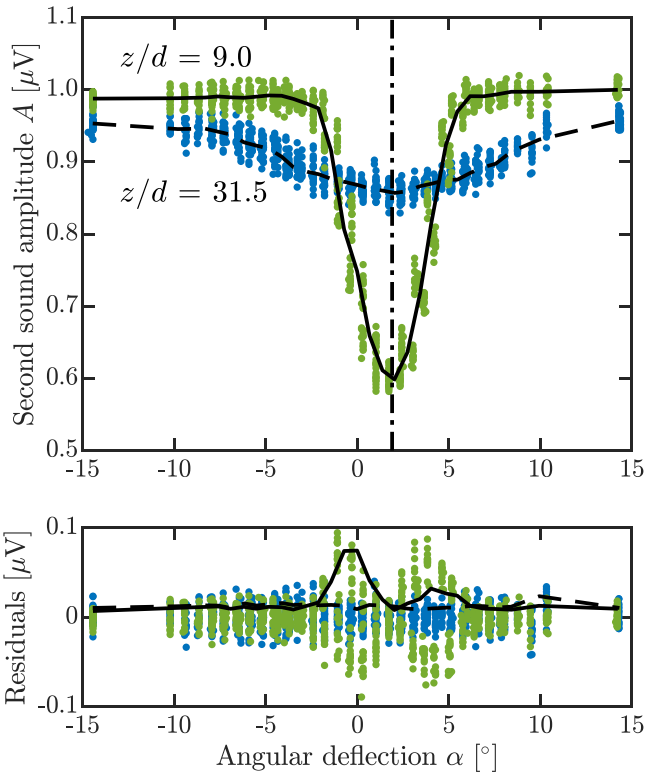

FIG. 4. Top panel: two sets of 30 sweeps (points) across the jet axis, obtained at 1.65 K and 776 mW (dataset A3) for $z/d = 9.0$ and 31.5, as indicated in the figure. Solid and dashed black lines: ensemble-averaged data used for the calculation of the quantized vortices' density. Dot-dashed black line: deflection offset $\alpha_0 \approx 1.9°$, Eq. (7). Bottom panel: residuals (points) and standard deviations (lines) corresponding to the data displayed in the top panel.

TABLE I. Summary of experimental conditions. T: temperature; P: heating power; v_n/η: normal fluid velocity inside the nozzle, Eq. (1); v_{ns}/η: counterflow velocity inside the nozzle, Eq. (2); Re/η: Reynolds number, Eq. (3). Note that the calculated values for the velocity and the Reynolds number can be seen as maximal theoretical values, obtained by assuming no heat leaks from the heater enclosure. In reality, the efficiency of the heat transfer through the nozzle is $\eta \lesssim 0.1$, as specified in the text.

Label	T (K)	P (mW)	v_n/η (m/s)	v_{ns}/η (m/s)	Re/η (10^3)
A1	1.65	194	0.78	0.97	175
A2	1.65	381	1.51	1.97	338
A3	1.64	776	3.24	3.98	726
B1	1.95	194	0.26	0.50	55
B2	1.95	381	0.52	0.99	108
B3	1.95	776	1.03	2.00	215
B4	2.10	776	0.65	2.40	107
C1	2.10	775	0.65	2.40	106
D1	1.66	240	0.92	1.15	206

Finally, the dataset D1 refers to the flow visualization study, whose bath temperature and heating power can be directly compared with sets A1 and A2. The dataset comprises approximately 1.88×10^6 particle position-velocity pairs, within the above-mentioned two-dimensional field of view.

For the measured values of T and P, see Table I, one can use Eqs. (1)–(3) to calculate nominal values of v_n, v_{ns}, and Re, assuming that the heat produced in the heater enclosure is transported toward the helium bath solely through the nozzle. In this idealized case, we obtain normal fluid and counterflow velocities of the order of 1 m/s, corresponding to Re values of the order of 10^5. These values are reported in Table I.

However, our 3D-printed enclosure is subjected to heat leaks, through its plastic walls and the joint between the enclosure and brass nozzle. The leaks are found to substantially reduce the flow velocity and the Reynolds number of the jets studied below. This claim can be directly verified via the visualization dataset, shown in Fig. 5.

In the left panel, we plot the mean particle velocity in the axial direction (color lines) as a function of the particle horizontal position in the field of view, corresponding to the radial direction. The dependence on the axial coordinate is specifically expressed by five offset lines, i.e., the $4d$ high field of view is split into five horizontal stripes, $0.8d$ high. At first glance, we can already say that the particle motions capture a spatially constrained flow structure. Outside the structure, the particles are practically still, while, inside it, they reach peak velocities of the order of 0.1 m/s. This value is in sharp contrast with the nominal values of v_n reported in Table I, which are about one order of magnitude larger than the experimental observation. Therefore, the actual normal fluid and counterflow velocities are at least one order of magnitude smaller than the maximum values estimated with Eqs. (1)–(3).

Heat leaks can be taken into account by assuming a finite efficiency $\eta \lesssim 0.1$ of the heat transfer through the nozzle. In particular, the heat flux through the nozzle q in Eq. (1) should become ηq, which means that the effective heating power is reduced to ηP in comparison with the values reported in Table I. However, providing a clear estimate of η based on the current data is not straightforward, also considering that the visualized region is not directly located above the nozzle, but approximately $5d$ away from it—note that in a previous study[34] it was found that, for an analogous setup, $\eta \approx 1/30$. We can nevertheless use the upper limits of v_n, v_{ns}, and Re reported in Table I to compare individual datasets, if we assume that η does not significantly change over the course of the experiment.

In order to investigate heat leaks in more detail, we placed a small germanium thermometer inside the enclosure and measured the temperature difference that develops between the enclosure and the bath after the heater is switched on. Time traces of the recorded temperature are presented in the left panel of Fig. 6 for a constant bath temperature of 1.30 K (note that the temperature difference is more

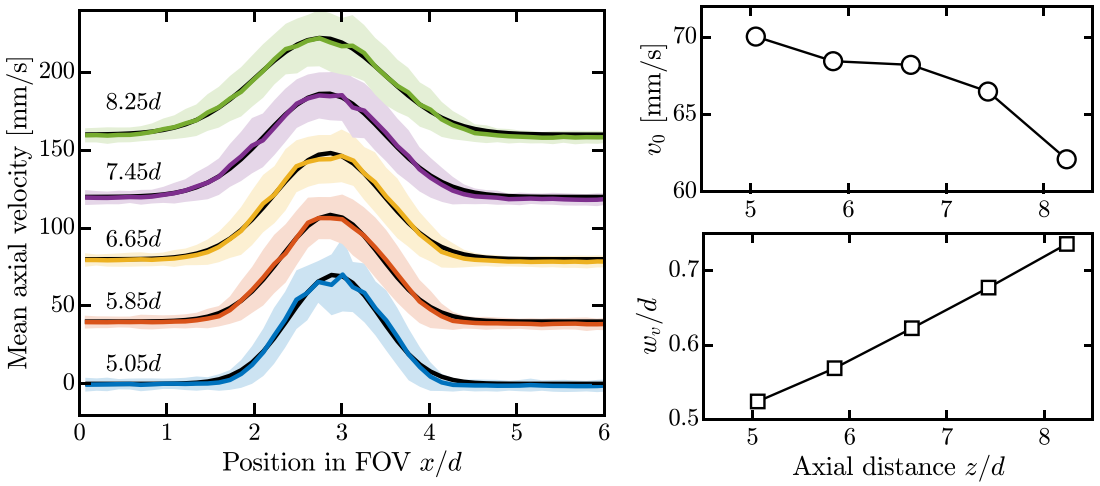

FIG. 5. Left panel: mean axial velocity of our solid particles, visualized in five regions, $0.8d$ high, crossing the jet axis (the curves are offset by 40 mm/s relative to each other). The distance separating each region center from the nozzle is specified next to each curve. A positive velocity indicates that the particles move, on average, away from the nozzle. Color lines: experimental data; pale color areas: one standard deviation intervals; black lines: Gaussian fits, Eq. (9); see also Sec. III A. Right panels: centerline velocity v_0 (top panel) and jet width w_v (bottom panel) as a function of the distance z from the nozzle, obtained from the Gaussian fits. Note that the quantities x, w_v, and z are normalized by the nozzle diameter d.

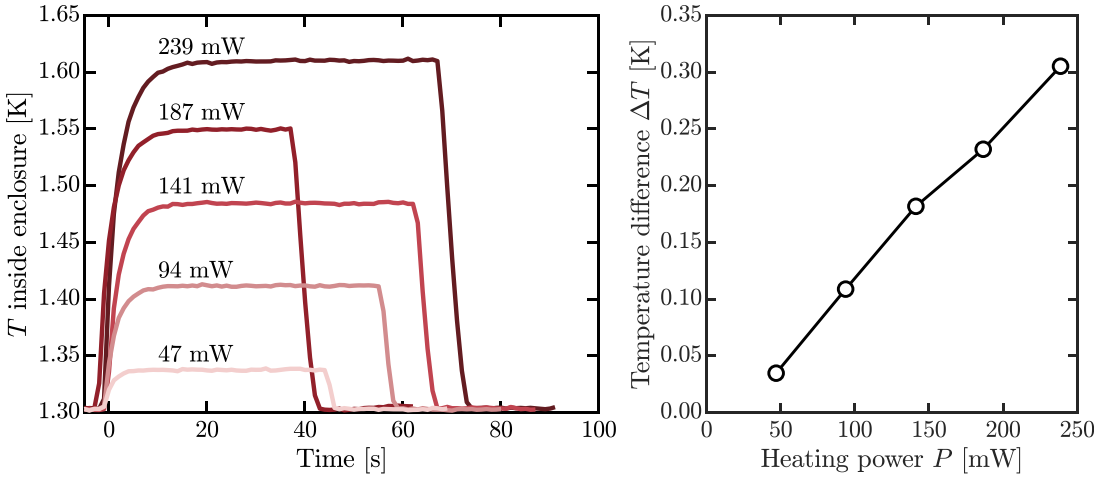

FIG. 6. Left panel: temperature inside the heater enclosure as a function of time. The bath temperature is kept constant at 1.30 K, and the heater is supplied by a constant heating power (specified near each curve) from approximately zero time. Right panel: steady temperature difference ΔT between the enclosure and the ^{4}He bath as a function of the heating power P.

prominent at lower temperatures because the heat capacity of He II is roughly proportional to p_n in the investigated temperature range). Specifically, for a set of rising heating powers, we observe that the heater enclosure warms up and reaches a steady state within a few seconds after the heater is powered. Once the heater is switched off, the enclosure quickly thermalizes with the surrounding bath.

First of all, it is apparent that the steady temperature difference ΔT between the enclosure and the ^{4}He bath is significant, of the order of 0.1 K. Additionally, the right panel of Fig. 6 displays ΔT as a function of the heating power P. We observe a neat linear dependence between these quantities, similar to Ref. 17, where it was also reported that, for counterflow jets, $\Delta T \propto q^3$ for $q \gtrsim 5$ kW/m^2. The latter is consistent with the data reported in Table I if we take into account the above-mentioned heat leaks, i.e., the results plotted in the right panel of Fig. 6 confirm that $\eta \lesssim 0.1$ in the range of investigated parameters because, otherwise, we should also see here the cubic scaling typical of turbulent counterflow in channels.[18] Nevertheless, the observed temperature difference leads to the formation of a prominent jet that features a dense tangle of quantized vortices. We now investigate this tangle using the second sound sensor as described above.

A. Spatial structure of the quantized vortices' tangle

The observed decrease in the second sound amplitude, indicating the presence of quantized vortices in the flow, depends on the radial and axial positions of the sensor, revealing the spatial structure of the quantized vortices' tangle associated with the counterflow jet. Figure 7

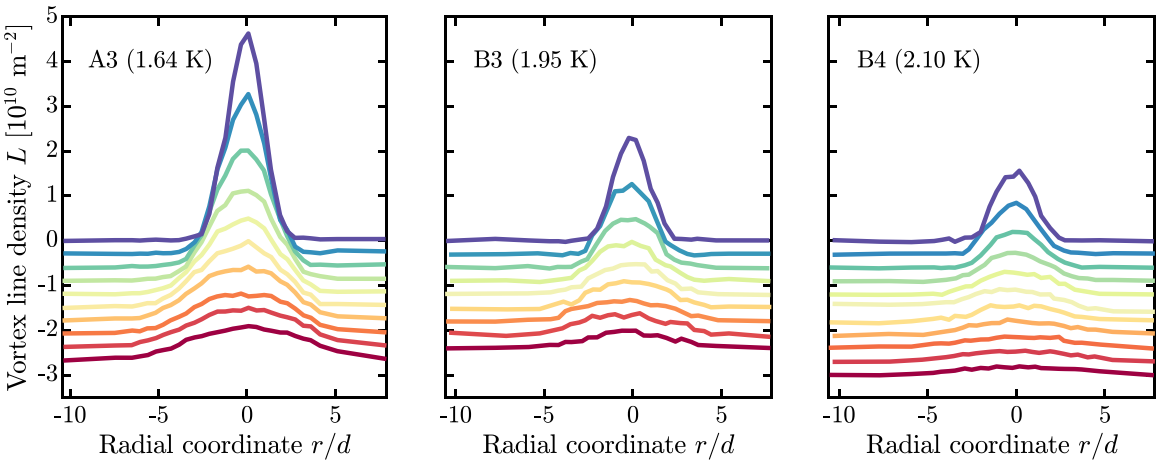

FIG. 7. Radial profiles of the vortex line density for $P \approx 776$ mW and different temperatures. The colors correspond to different axial positions of the sensor, from $9d$ above the nozzle (dark blue) to $31.5d$, $29d$, and $34d$ (dark red) for the left, middle, and right panels, respectively, with steps of $2.5d$. The curves are offset by 3×10^9 m^{-2} for the sake of clarity. Positive and negative values of the radial coordinate r, here normalized by the nozzle diameter d, denote the corresponding angular deflection ($r/d < 0$ means $\alpha < \alpha_0$ and vice versa).

displays the vortex line density L, also named VLD below, calculated from Eq. (6), for datasets A3, B3, and B4. These datasets are characterized by the same heating power ($P \approx 776$ mW) and different temperatures. The individual curves correspond to different axial distances, starting from $9d$ (dark blue) above the nozzle, up to $31.5d$, $29d$, and $34d$ (dark red), for sets A3, B3, and B4, respectively—the curves are vertically offset for clarity. These radial VLD profiles map the quantized vortices' tangle in unprecedented detail, and we specifically observe the tangle to be spatially confined and growing in the radial direction—considering the errors discussed above, we remind that individual L values are here given with relative uncertainty equal to approximately 10%.

Moreover, the highest L values are obtained for the smallest axial distances and for the lowest temperature. A similar temperature dependence is displayed by the normal fluid velocity v_n for a constant heating power, i.e., v_n increases as T decreases—see Eq. (1). On the other hand, v_{ns} is not a monotonous function of temperature and, for the displayed data, the smallest v_{ns} is obtained for 1.95 K—see Eq. (2) and Table I. Specifically, this discrepancy between the temperature dependencies of VLD and v_{ns} tells us that the physical mechanisms resulting in the formation of counterflow jets are different from those taking place in ordinary channel counterflow, where the scaling $L \propto v_{ns}^2$ was consistently observed for a rather wide range of temperatures and counterflow velocities.[35] In other words, our data support the picture that the quantized vortices' tangle associated with the jet is not simply generated in the nozzle, where channel counterflow takes place, and subsequently ejected into the volume above it. In particular, as discussed below, we find the quantized vortices' tangle to possess properties that are usually attributed to turbulent coflow of He II, i.e., to a configuration where the two fluid components are locked together in a single velocity field.

The obtained VLD profiles can be fitted with a Gaussian peak of the form

$$L(r) = L_0 \exp\left[-\left(\frac{r}{w}\right)^2\right], \tag{8}$$

where the peak amplitude L_0 and width w are taken as fitting parameters to match the experimental data. The Gaussian-like shape of our VLD profiles is reminiscent of the bell-shaped profile of the vorticity magnitude inferred in a classical round jet using the particle imaging velocimetry technique,[36] and it is equally reminiscent of the bell-shaped profile of the energy dissipation inferred from hot wire anemometry measurements in a similar flow.[37] Note in passing that, under the assumption of homogeneous and isotropic turbulence, energy dissipation and squared vorticity are proportional to each other,[38] but, at the same time, one should keep in mind that quantities having similar Gaussian-like statistical distributions are not necessarily related from a physical point of view.

It is now useful to mention that the profiles of the axial velocity, presented in the left panel of Fig. 5, display a spatial structure similar to that of the VLD profiles. In direct analogy with Eq. (8), we then fit individual velocity profiles using

$$v(x) = v_0 \exp\left[-\left(\frac{x}{w_v}\right)^2\right], \tag{9}$$

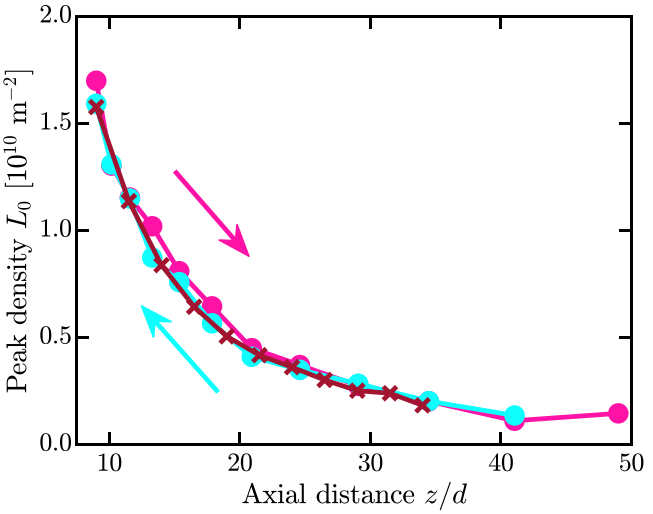

FIG. 8. Peak vortex line density (i.e., density along the jet axis) L_0 as a function of the axial distance z, normalized by the nozzle diameter d, for datasets B4 (red crosses) and C1 (cyan and magenta points). Color arrows denote the direction of the sensor stroke (receding from or approaching toward the nozzle).

where the fitting parameters are the centerline velocity v_0 and the jet width w_v. Specifically, the left panel of Fig. 5 shows the close agreement between the experimental data (color lines) and the fitting function (black lines), and the axial dependence of both fitting parameters is displayed in the two panels on the right.

Additionally, to highlight the effect of our sensor motion on the investigated flow, we compare in Fig. 8 the L_0 values obtained by fitting the full VLD profiles of dataset B4 (red crosses) with the directly measured peak values of dataset C1 (points) as a function of z/d—note that dataset C1 includes two axial strokes of the sensor. The L_0 values detected by the sensor that gradually moves toward the nozzle are marked by cyan points, and the magenta points denote data taken by the sensor that moves in the opposite direction. The curves closely overlap within the full range of investigated distances and within the accuracy of the experimental technique, which neatly illustrates that our observations are fully reproducible.

B. Scaling of the vortex line density

We now analyze how the peak amplitude L_0 and width w of individual VLD profiles scale with the axial distance z. First of all, the relation between L_0 and z/d is presented in Fig. 9 for datasets A1–A3 and B1–B4, marked by open symbols (we also use this notation in the following figures). Here, no artificial vertical shift is imposed, and the vertical distribution of data lines is given by different experimental conditions, listed in Table I.

The observed $L_0(z)$ dependencies are compatible with power laws, with exponents ranging from -2 to $-3/2$, as indicated by the black lines in the figure. Specifically, the former exponent is found to match relatively small peak densities, while the latter one fits relatively dense tangles. Since the centerline velocity $v_0 \propto z^{-1}$ holds for both classical and counterflow jets,[23,25] it apparently follows that $L_0 \propto v_0^{3/2}$ for the largest line densities, while the $L_0 \propto v_0^2$ dependence holds for

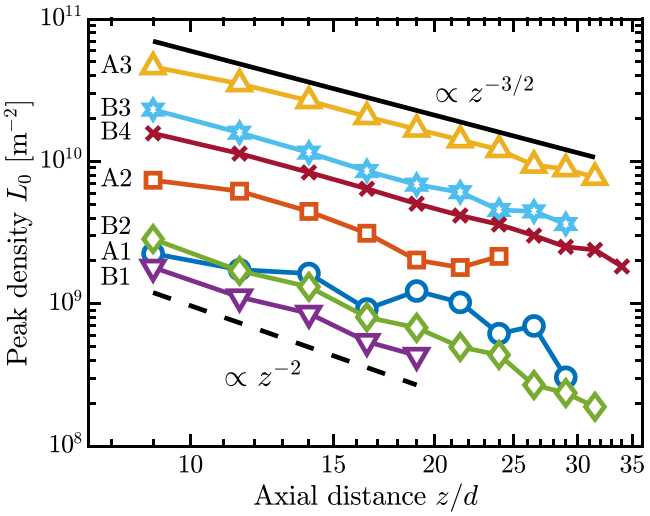

FIG. 9. Peak vortex line density L_0 as a function of the normalized axial distance z/d. Dataset labels are indicated to the left of each curve. Note the log–log scale.

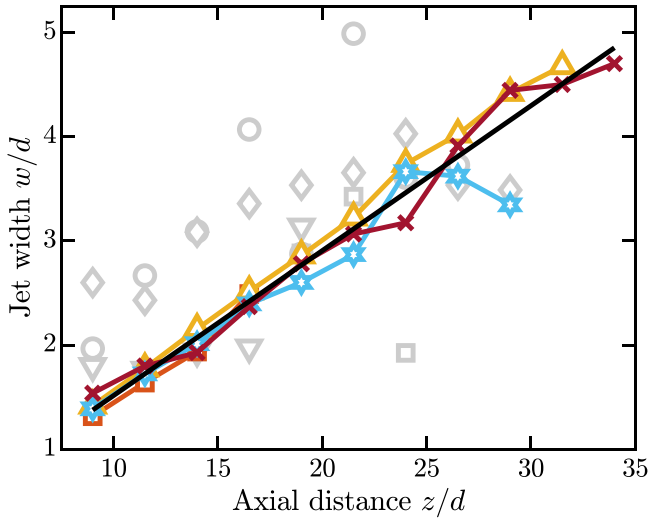

FIG. 10. Peak width w as a function of the axial distance z (both quantities are normalized by the nozzle diameter d). Color symbols: points with $L_0 > L_t$, i.e., datasets A2 (in part), A3, B3, and B4, collectively named high set; gray symbols: remaining points, with $L_0 \leq L_t$, i.e., datasets A1, A2 (in part), B1, and B2, collectively named low set. Note that the symbols are as in Fig. 9, regardless of their color; black line: linear fit, Eq. (10).

the smallest ones observed in our experiment. Two alternative interpretations of this puzzling behavior are discussed in Sec. IV.

Note in passing that our visualization data (see the top right panel of Fig. 5) do not seem to reproduce the expected scaling of the centerline velocity, although the latter does show the tendency to decrease as the axial distance increases. The mismatch can be attributed to the fact that the jet flow was visualized in the near field region, extending up to approximately $7d$ away from the nozzle,[24] where the mentioned scaling law is actually not expected to hold.

The axial dependence of the peak width w is plotted in Fig. 10. The data points characterized by a relatively large VLD amplitude display a neat linear dependence of w with z, which is also independent of experimental parameters, see colored points in Fig. 10. We identify these well-resolved VLD peaks by setting a threshold $L_t = 2.2 \times 10^9$ m^{-2}. This value is chosen so that $L_{\min}/L_t \approx 0.05$, i.e., it holds that the profiles meeting this threshold density display VLD values larger than $L_{\min}$, at least within the interval $[-2w, 2w]$, which is required for a well-converged Gaussian fit and a reliable estimation of the fitting parameters. Additionally, the errors associated with the w estimates, which are computed from 95% confidence bounds of the fit, range from 2% to 6% for the well-resolved data, and the similarly obtained errors of L_0 are between 1% and 5%. For the datasets that fail to meet the threshold value L_t, the relative errors of w estimates are as high as 33%—and those of L_0 are as high as 22%. In the following, for the sake of brevity, the colored points in Fig. 10, those with $L_0 > L_t$, are named high (data) set, while the others are called low (data) set, because, as already noted, they can be, respectively, associated with high and low values of peak density—see again Fig. 9.

We fit the widths corresponding to the high set together using

$$w(z) = \beta_L (z - z_0), \tag{10}$$

where we find that the virtual origin $z_0 \approx -0.9d$ and that the growth rate $\beta_L = \mathrm{d}w/\mathrm{d}z$ of the vortex tangle is equal to approximately 0.14 (see the solid black line overlaying the experimental data in Fig. 10). Similar values are reported for the velocity field of classical round jets. For example, the jet's virtual origin is found to be rather close to the nozzle also in Ref. 37. Additionally, Ref. 1 reports a linear growth of the velocity profile, with a rate $\beta = 0.11$, for Re $\approx 10^5$, and in Ref. 39, a similar value is given for Re $\approx 10^4$. For the sake of comparison, it is also useful to estimate the full width at half maximum (FWHM) of the VLD profile, and, for a Gaussian peak, we obtain $\beta_L^{\mathrm{FWHM}} = 2\sqrt{\log 2}\beta_L \approx 0.23$, which, once more, is a value comparable to the FWHM-based growth rate of approximately 0.21, reported in Ref. 27. However, one should keep in mind that velocity and vortex line density profiles are expected to be different in nature, e.g., the widths of velocity and VLD profiles are not expected in general to grow at the same rate, and, on top of this, counterflow and classical jets are characterized by different production mechanisms, which should shift the virtual origins. Note, finally, that the bottom right panel of Fig. 5 presents the width of the velocity profiles vs the axial distance z/d, obtained from our flow visualization measurements in He II. Here again, we find an affine growth of the velocity profile width, consistent with that of classical jets.

In summary, the emergence of approximately Gaussian profiles for the vortex line density, alongside with the scaling laws outlined above, suggests that the quantized vortices' tangle develops a structure that is tightly coupled to the associated velocity field, at least within the intermediate field region of the jet. In other words, the quantized vortices' tangle grows in size, while decreasing its peak density with z, similarly as the peak flow velocity that decreases with z, due to turbulent entrainment and momentum conservation.

IV. DISCUSSION

In the following, we outline two interpretations of the just presented experimental results. The first one, detailed in Sec. IV A and proposed by P. Švančara and P.-E. Roche, leads us to conjecture a self-

similar functional form of the vortex tangle density across counterflow jets. The other, detailed in Sec. IV B and proposed by M. La Mantia, suggests that the position of the superfluid stagnation point could depend on the flow forcing as well. Both interpretations can be used to explain in part the obtained results.

A. Self-similar jet model

It is apparent from Figs. 9 and 10 that the curves associated with the smallest peak densities, corresponding to the low set, defined in Sec. III B, are characterized by a larger scatter in comparison with the other curves. This can be attributed to the less accurate fit of Eq. (8) to weakly attenuated second sound signals, i.e., to relatively low values of L, especially in the off-axis region. In view of improving the statistical convergence, we introduce here an alternative, dimensionless quantity, $\mathcal{L}_z$, which aggregates a larger set of measurements. Specifically, if we assume that the distribution of quantized vortices in the jet is axially symmetric, i.e., that L is independent of the azimuthal coordinate ϕ, we calculate this quantity, the cumulative length of quantized vortices per unit height, as

$$\mathcal{L}_z(z) = \int_0^\infty \int_0^{2\pi} L(r,z) r \mathrm{d}r\mathrm{d}\phi = \int_0^\infty 2\pi r L(r,z)\mathrm{d}r. \tag{11}$$

Additionally, we note from Fig. 10 that the VLD profiles associated with the high set are self-similar, at least in the range of investigated parameters. This self-preserving property of jets far away from the nozzle is well known for classical jets,[38] and it was also invoked to interpret previous experiments on counterflow jets.[9] This implies that the (high set) VLD profiles can be modeled as

$$L(r,z) = \mathcal{G}\left(\frac{r}{z-z_0}\right) L_0(z) = \mathcal{G}(x) L_0(z), \tag{12}$$

where the dimensionless profile shape $\mathcal{G}(x)$ can be approximated, for example, by a Gaussian peak, ensuring that $\mathcal{G}(0) = 1$. Equations (11) and (12) then lead to the scaling relation

$$\mathcal{L}_z(z) = (z-z_0)^2 L_0(z) \int_0^\infty 2\pi x \mathcal{G}(x)\mathrm{d}x \propto z^2 L_0(z), \tag{13}$$

where we assume that the integral is finite and that $z_0 \ll z$. Equation (13) shows us how $\mathcal{L}_z$ and L_0 are related under the self-similarity hypothesis.

The cumulative vortex length $\mathcal{L}_z$ can be estimated from the experimental data in two different ways. The first one consists in using the full VLD profiles, e.g., those presented in Fig. 7. We can then numerically estimate the right-hand side of Eq. (11) within the limits $(r_{\min}, 0)$ or $(0, r_{\max})$, where $r_{\min}$ ($r_{\max}$) is the minimum (maximum) radial coordinate probed by the sensor. Since the obtained radial profiles fully capture the region occupied by the quantized vortices' tangle, as shown, e.g., in Fig. 7, these integrals adequately approximate Eq. (11)—note that, to reduce error, we take as the final estimate of $\mathcal{L}_z$ for this first method the average value of the integrals with $r_{\min}$ and $r_{\max}$. The second approach relies on the explicit form of $\mathcal{G}$ introduced above to model the high set profiles. In agreement with Eqs. (8) and (10), we set

$$\mathcal{G}\left(\frac{r}{z-z_0}\right) = \exp\left\{-\left[\frac{r}{\beta_L(z-z_0)}\right]^2\right\} = \exp\left[-\left(\frac{r}{w}\right)^2\right] \tag{14}$$

and evaluate the integral on the right-hand side of Eq. (11) as

$$\mathcal{L}_z = 2\pi L_0 \int_0^\infty \exp\left[-\left(\frac{r}{w}\right)^2\right] r\mathrm{d}r = \pi L_0 w^2. \tag{15}$$

Both estimates of $\mathcal{L}_z$ are presented in Fig. 11 as a function of the axial distance z. The left panel represents the right-hand side of Eq.

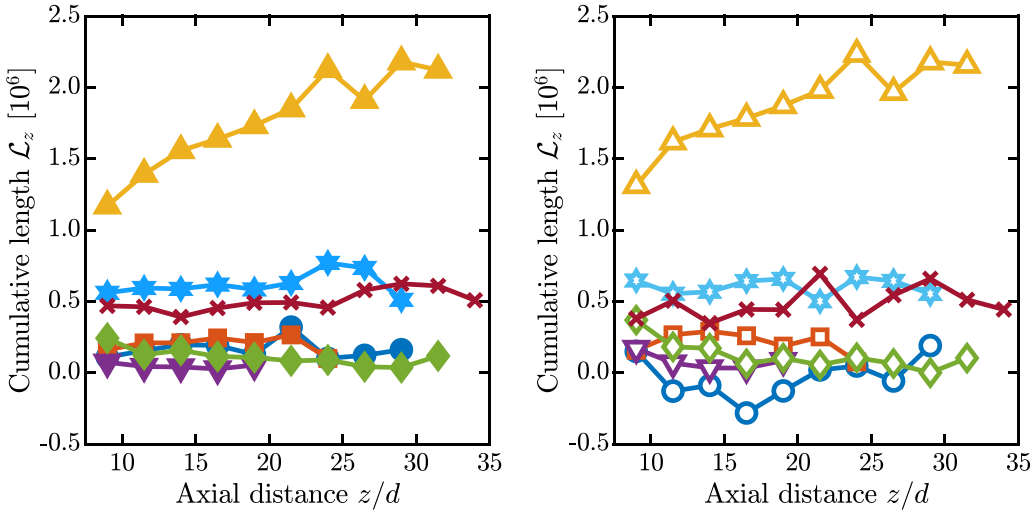

FIG. 11. Cumulative length $\mathcal{L}_z$ of quantized vortices per unit height as a function of the normalized axial distance z/d. Left panel: right-hand side of Eq. (15), computed using the experimentally obtained values of L_0 and w. Right panel: result of the numerical integration of the right-hand side of Eq. (11) as discussed in the text. Colors as in Fig. 9.

(15), and the right panel displays the result of the numerical integration of the right-hand side of Eq. (11) using the trapezoidal rule. The two methods yield comparable results except for dataset A1 (open blue circles, right panel), where the nonphysical, negative values of $\mathcal{L}_z$ most likely result from the poor signal-to-noise ratio (a negative vortex line density is obtained from Eq. (6) when $A > A_0$). Note again that Eq. (15) is derived assuming that the studied flows are self-similar.

It is apparent from Fig. 11 that, for a given heating power P and helium bath temperature T, i.e., for a given dataset, the cumulative length $\mathcal{L}_z$ does not depend on z within the experimental uncertainty and for all datasets but one. Taking Eq. (13) into account, we can therefore say that $L_0(z) \propto z^{-2}$ in the range of investigated parameters, excluding dataset A3 (yellow triangles). In this case, $\mathcal{L}_z$ grows with the axial distance z, which is an unexplained exception. Nevertheless, leaving this dataset aside for the moment, it now seems that the variations of the power-law exponents apparent in Fig. 9 are compensated by suitable changes in the growth of the measured VLD profile width, presented in Fig. 10. This compensation could be explained, at least in part, by stochastic fluctuations of the jet direction. The latter could systematically decrease the measured centerline density of quantized vortices and simultaneously increase the measured jet width. Apparently, the use of the cumulative vortex length allows us to largely discard the data scatter observed in Figs. 9 and 10.

The inverse quadratic scaling of $L_0(z)$ has a straightforward interpretation using a heuristic relation tested by numerical simulations and experiments in steady, nearly homogeneous coflow of turbulent He II.[40,41] These works relate L_c, the mean density of the quantized vortices' tangle in coflow, and the energy dissipation rate ε as

$$L_c^2 \propto \varepsilon \propto \frac{v_{\mathrm{rms}}^3}{H}, \tag{16}$$

where v_{rms} is the root mean square velocity of the coflow being investigated, and H indicates a velocity correlation distance usually called the integral length scale.

Turbulence along the axis of classical round jets can be locally approximated as homogeneous and isotropic,[38] and some local properties of turbulence can be inferred from the local values of v_{rms} and H, as shown, for example, in Refs. 42–44. Specifically, following this reasoning, one can estimate along the jet axis the vorticity magnitude and the energy dissipation rate, appearing in the classical relation analogous to Eq. (16). In other words, we assume here that Eq. (16) holds locally on the counterflow jet axis, with $L_c \equiv L_0$ (note that in Ref. 9 the assumptions of local homogeneity and isotropy have been already used to interpret measurements of the second sound waves crossing a counterflow jet).

In particular, for a given dataset, and taking into account the empirical scaling relations $v_{\mathrm{rms}} \propto v_0$ and $H \propto w \propto z$, Eq. (16) becomes

$$L_0^2 \propto \frac{v_0^3}{w} \propto \frac{z^{-3}}{z} \propto z^{-4}, \tag{17}$$

which fully accounts for the observed inverse quadratic scaling of L_0 with z. Additionally, for a fixed temperature, we can write that

$$L_0(z, P) \approx z^{-2}\mathcal{F}(P), \tag{18}$$

where $\mathcal{F}$ is an unknown function of the heating power.

Now, in view of further reducing our data scatter, we take advantage of the conjectured invariance of $\mathcal{L}_z$ along the jet axis and we calculate its average value—the averaging operator is denoted as $\langle \cdot \rangle_z$ and the average value is, therefore, $\langle \mathcal{L}_z \rangle_z$. Figure 12 shows $\langle \mathcal{L}_z \rangle_z$, computed from the data displayed in the left panel of Fig. 11, as a function of the heating power—the dotted lines connect points corresponding to the same bath temperature. Although the data scatter—likely due to experimental errors and temperature dependence—is not negligible, we find that $\langle \mathcal{L}_z \rangle_z$ roughly follows a $P^{3/2}$ scaling (black line) that ought to be interpreted. Assuming that the dimensionless VLD profile shape $\mathcal{G}$ is independent of P, we find from Eqs. (13) and (18) that

$$\langle \mathcal{L}_z \rangle_z \propto \langle z^2 L_0(z, P) \rangle_z \approx \mathcal{F}(P). \tag{19}$$

What now remains is to understand why $\mathcal{F} \propto P^{3/2}$. At any given z, it results from the proportionality between L_0^2 and v_0^3 in turbulent coflows,[40,41] which is apparent from Eq. (17). Due to the counterflow generation mechanism, Eq. (1), the centerline velocity v_0 scales linearly with P (or ηP to account for heat losses). We, therefore, obtain $\mathcal{F} \propto L_0 \propto v_0^{3/2} \propto P^{3/2}$, consistently with the outcome of Fig. 12.

It is now useful to mention Ref. 19, where an elongated counterflow jet of He II was investigated at a distance of approximately 10 nozzle widths from the flow source using a second sound beam traveling across the jet. For temperature (1.6–2.1 K) and heat flux (3–50 kW/m^2) ranges comparable to those of the present work, the attenuation factor, which is proportional to the vortex line density, was reported to scale as P^k with $k = 1.3$–1.6. The outcome was later explained using geometrical acoustics, assuming that the counterflow jet is turbulent and that the normal and superfluid components are locked in a single velocity field.[9]

To summarize, excluding dataset A3 that remains to be understood, our results are consistent with a self-similar spatial distribution of the quantized vortex tangle, whose density L can be written as

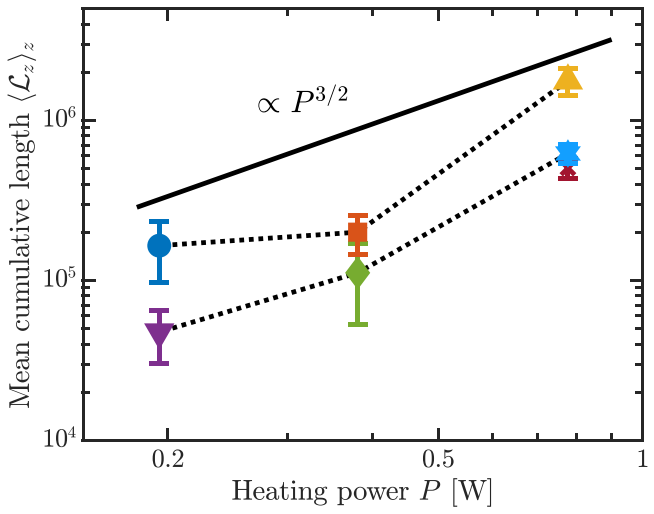

FIG. 12. Mean cumulative length $\langle \mathcal{L}_z \rangle_z$ as a function of the heating power P. Colors as in Fig. 9; error bars correspond to one standard deviation interval. Black dotted lines connect data points collected at the same temperature of the helium bath.

$$L(r,z,P) \propto \frac{P^{3/2}}{z^2}\mathcal{G}\left(\frac{r}{z-z_0}\right), \tag{20}$$

where $\mathcal{G}$ is a Gaussian-like function. If we substitute for $\mathcal{G}$ the employed Gaussian fit, we obtain an explicit functional form, i.e.,

$$L(r,z,P) \propto \frac{P^{3/2}}{z^2}\exp\left\{-\left[\frac{r}{\beta_L(z-z_0)}\right]^2\right\}, \tag{21}$$

where the z^{-2} factor accounts for the linear development of the integral scale along the jet, far away from the nozzle. Now, for consistency with the exponential term, the jet virtual origin can be reintroduced in this factor, to better account for smaller z, see Eq. (13).

Additionally, although the determination of the temperature dependence is not possible on the basis of the present data, three physical arguments suggest how to make it explicit. First of all, the spreading rate of classical jets is due to the balance between mixing and axial entrainment, and these processes should remain equally efficient in He II when both components are flowing together. Therefore, we expect that β_L will have a weak dependence on T and P. On the contrary, the virtual origin z_0 can be associated with the crossover from the counterflow to the coflow regime, and we then expect it to explicitly depend on T and P. Finally, the amount of quantized vortex lines generated in a given He II coflow depends on temperature, because the vortex dynamics depends on the normal fluid fraction,[19] which is strongly temperature dependent, see again Fig. 1—one can then embed the latter consideration into an unknown function of temperature, $\mathcal{T}$.

Following the previous reasoning, we can consequently write a generalized version of Eq. (21), i.e.,

$$L(r,z,P,T) \approx \frac{P^{3/2}}{[z-z_0(P,T)]^2}\exp\left\{-\left[\frac{r}{\beta_L[z-z_0(P,T)]}\right]^2\right\}\mathcal{T}(T), \tag{22}$$

where z is large compared to z_0, to meet the self-similarity condition, $\beta_L \approx 0.14$, and $z_0 \approx -0.9d$, as reported above. We remind, however, that the numerical values might be biased by the response of the second sound sensor to the flow velocity; that is, we assume in this work that the contribution of the fluid velocity to second sound attenuation is not significant. More generally, further studies are required to quantitatively validate the proposed model, e.g., to understand why the $\mathcal{L}_z$ vs z scaling differs for dataset A3 compared to the others.

B. Moving stagnation point interpretation

In Sec. III B, we reported that the $L_0(z)$ dependencies plotted in Fig. 9 are compatible with power laws, with exponents ranging from -2 to $-3/2$. Specifically, the former exponent can be associated with relatively small peak densities, i.e., to the low set, while the latter one is more suitable for relatively denser tangles, i.e., for the high set. Considering that $v_0 \propto z^{-1}$ is expected to hold for self-similar round jets, one can then derive $L_0 \propto v_0^{3/2}$ for the largest line densities, while the $L_0 \propto v_0^2$ scaling is more adequate for the smallest ones.

As already mentioned, the 3/2-power scaling was reported in previous studies—see, e.g., Refs. 9 and 35—and can be associated with turbulent coflow of He II. More precisely, one can derive it from Eq. (16) assuming that the integral length scale H does not depend locally on other flow scales. This could happen in the region where the hypothesis of locally homogeneous and isotropic flow is expected to hold, i.e., along the jet axis, where no information on the jet width w should be accessible, if the typical size of this region is smaller than w—note again that $H \propto w$ for self-similar jets. In other words, the assumption made in this section is that the integral length scale H is constant in the region where Eq. (16) holds.

The 2-power scaling is instead often associated with channel counterflow, i.e., $L \propto v_{ns}^2$, as discussed, e.g., in Ref. 35. However, as already noted in Sec. III A, the normal fluid and counterflow velocities are in general not directly proportional to each other, but this is only true at liquid temperatures higher than approximately 2 K (Ref. 7). It then follows that, at lower temperatures, $v_n \propto v_{ns}$. Additionally, considering that, as reported in Sec. IV A, v_0 should be proportional to v_n, we find that $L_0 \propto v_0^2$ for our more dilute tangles, i.e., for the low set, collected at temperatures lower than 2 K.

From this discussion, one can then say that, at sufficiently low values of heating power, channel counterflow features could also be observed in counterflow jets. The physical reason could be related to the mutual friction force, which can be seen as an energy sink. Specifically, this dissipation mechanism could become inefficient for counterflow jets at sufficiently high values of heating power. In other words, the position of the stagnation point depicted in Fig. 2 could be a function of the heating power and move closer to the nozzle as the power increases.

The suggestion appears a bit less adventurous if one considers that counterflow jets at relatively low heating power have yet to the thoroughly investigated or at least they have received to date less attention than those at higher heating power. Indeed, we reported in Sec. III that, on the basis of Ref. 17, we expect ΔT to be linearly proportional to q in the range of parameters probed here, while this is not the case of other studies on counterflow jets, such as Refs. 14 and 16, where a neat cubic scaling was observed at larger values of heat flux. Specifically, Refs. 17 and 21 are apparently the only works where some attention is given to the just mentioned linear regime and, more importantly, the claim that the superfluid stagnation point is located in the close proximity of the nozzle is solely based on data collected in the cubic regime, i.e., at relatively high values of heating power.

Finally, it is useful to mention that, from the right-hand side of Eq. (15) and the $L_0 \propto v_0^{3/2}$ scaling, one can get that $\mathcal{L}_z$ should be proportional to $z^{1/2}$, at least for the high set. However, in Fig. 11, we observe that $\mathcal{L}_z$ grows with the axial distance z only for dataset A3, corresponding to the largest Reynolds number, while this is not the case for the other datasets displaying the proportionality between w and z. Once more, further experiments are required to assess the validity of the physical interpretations presented here.

V. CONCLUSIONS

The intermediate field region of round counterflow jets, representing a unique type of thermally driven flow of He II, was studied in the turbulent regime, for Reynolds numbers of the order of 10^4, using the second sound attenuation and flow visualization techniques. Specifically, a miniature second sound sensor was employed to detect the vortex line density across the jet axis, with a spatial resolution slightly larger than the nozzle diameter, at fluid temperatures between 1.64 and 2.10 K—note, however, that the measured density is biased by an additional sensitivity of the employed second sound sensor to the flow velocity, which cannot be precisely quantified at the moment.

Nevertheless, within the range of investigated axial distances, from 9 to 34 nozzle diameters, we observe a highly inhomogeneous tangle of quantized vortices. In particular, the vortex line density displays a Gaussian-like profile in the radial direction and, for the highest density values, its width w grows linearly with the axial distance z at a rate $\mathrm{d}w/\mathrm{d}z \approx 0.14$, which is comparable but not equal to the radial growth rate observed for the classical velocity field—similar remarks apply to the jet virtual origin. Additionally, as shown in Fig. 9, the peak density of the quantized vortices' tangle appears to follow, as a function of the axial distance, power laws with exponents ranging approximately between -2 and $-3/2$. Two physical interpretations of the observed scaling behavior are proposed, and none of them account for all the measured datasets. One interpretation conjectures a general functional form of the vortex line density in counterflow jets, which depends on spatial coordinates and heating power. The other suggests that the position of the superfluid stagnation point along the jet axis could depend on the heating power as well.

In summary, the present work indicates that future studies on counterflow jets should be devoted to extend the ranges of experimental parameters accessed to date, e.g., in order to quantitatively identify the conditions in which jet flows of superfluid ^{4}He are appreciably different from their classical analogs.

ACKNOWLEDGMENTS

We thank Jerôme Valentin for microfabricating parts of the employed second sound sensor. We are also thankful to Eric Woillez and the technical staff of Institut Néel for their prompt assistance during the second sound experiments, performed in Grenoble by P. Švančara and P.-E. Roche—the visualization and thermometry experiments were performed in Prague by P. Švančara and M. La Mantia. P.-E. Roche acknowledges support from the ANR QUTE-HPC grant (No. ANR-18-CE46-0013) and the EU Horizon 2020 program The European Microkelvin Platform (EMP 824109). P. Švančara and M. La Mantia were supported in part by the Czech Science Foundation (GAČR) under Grant No. 19-00939S. P. Švančara also acknowledges the Barrande Fellowship Programme supporting doctoral mobility. Additionally, during the manuscript preparation in 2022, M. La Mantia was in part supported by the Czech Science Foundation (GAČR) under Grant No. 20-00918S.

AUTHOR DECLARATIONS

Conflict of Interest

The authors have no conflicts to disclose.

Author Contributions

All authors contributed equally to this work.

Patrik Švančara: Conceptualization (equal); Data curation (equal); Formal analysis (equal); Funding acquisition (equal); Investigation (equal); Methodology (equal); Project administration (equal); Resources (equal); Software (equal); Supervision (equal); Validation (equal); Visualization (equal); Writing – original draft (equal); Writing – review & editing (equal). **Philippe-Emmanuel Roche:** Conceptualization (equal); Data curation (equal); Formal analysis (equal); Funding acquisition (equal); Investigation (equal); Methodology (equal); Project administration (equal); Resources (equal); Software (equal); Supervision (equal); Validation (equal); Visualization (equal); Writing – original draft (equal); Writing – review & editing (equal). **Marco La Mantia:** Conceptualization (equal); Data curation (equal); Formal analysis (equal); Funding acquisition (equal); Investigation (equal); Methodology (equal); Project administration (equal); Resources (equal); Software (equal); Supervision (equal); Validation (equal); Visualization (equal); Writing – original draft (equal); Writing – review & editing (equal).

DATA AVAILABILITY

The data that support the findings of this study are available from the corresponding author upon reasonable request.

REFERENCES

[1]I. Wygnanski and H. Fiedler, "Some measurements in the self-preserving jet," J. Fluid Mech. **38**, 577–612 (1969).
[2]D. Durì, J. Salort, P. Diribarne, P.-E. Roche, and C. Baudet, "Vorticity scattering measurements in a superfluid inertial round jet," J. Phys. Conf. Ser. **318**, 092027 (2011).
[3]C. F. Barenghi, L. Skrbek, and K. R. Sreenivasan, "Introduction to quantum turbulence," Proc. Natl. Acad. Sci. U. S. A. **111**, 4647–4652 (2014).
[4]M. S. Mongiovì, D. Jou, and M. Sciacca, "Non-equilibrium thermodynamics, heat transport and thermal waves in laminar and turbulent superfluid helium," Phys. Rep. **726**, 1–71 (2018).
[5]L. Landau, "Theory of the superfluidity of helium II," Phys. Rev. **60**, 356–358 (1941).
[6]R. J. Donnelly, "The two-fluid theory and second sound in liquid helium," Phys. Today **62**(10), 34–39 (2009).
[7]R. J. Donnelly and C. F. Barenghi, "The observed properties of liquid helium at the saturated vapor pressure," J. Phys. Chem. Ref. Data **27**, 1217–1274 (1998).
[8]R. J. Donnelly, *Quantized Vortices in Helium II* (Cambridge University Press, 1991).
[9]H. W. Liepmann and G. A. Laguna, "Nonlinear interactions in the fluid mechanics of helium II," Ann. Rev. Fluid Mech. **16**, 139–177 (1984).
[10]J. Bertolaccini, E. Lévêque, and P.-E. Roche, "Disproportionate entrance length in superfluid flows and the puzzle of counterflow instabilities," Phys. Rev. Fluids **2**, 123902 (2017).
[11]M. La Mantia, "Particle dynamics in wall-bounded thermal counterflow of superfluid helium," Phys. Fluids **29**, 065102 (2017).
[12]P. Hrubcová, P. Švančara, and M. La Mantia, "Vorticity enhancement in thermal counterflow of superfluid helium," Phys. Rev. B **97**, 064512 (2018).
[13]P. Švančara, P. Hrubcová, M. Rotter, and M. La Mantia, "Visualization study of thermal counterflow of superfluid helium in the proximity of the heat source by using solid deuterium hydride particles," Phys. Rev. Fluids **3**, 114701 (2018).
[14]M. Murakami and N. Ichikawa, "Flow visualization study of thermal counterflow jet in He II," Cryogenics **29**, 438–443 (1989).
[15]G. Careri, M. Cerdonio, and F. Dupré, "Vorticity in liquid He II flow through orifices," Phys. Rev. **167**, 233–238 (1968).
[16]P. E. Dimotakis and J. E. Broadwell, "Local temperature measurements in supercritical counterflow in liquid helium II," Phys. Fluids **16**, 1787–1795 (1973).
[17]M. Murakami, T. Yamakazi, and H. Nakai, "Laser Doppler velocimeter measurements of thermal counterflow jet in He II," Cryogenics **29**, 1143–1147 (1989).
[18]C. J. Gorter and J. H. Mellink, "On the irreversible processes in liquid helium II," Phys. **15**, 285–304 (1949).
[19]G. A. Laguna, "Second-sound attenuation in a supercritical counterflow jet," Phys. Rev. B **12**, 4874–4881 (1975).
[20]P. E. Dimotakis and G. A. Laguna, "Investigations of turbulence in a liquid helium II counterflow jet," Phys. Rev. B **15**, 5240–5244 (1977).
[21]A. Nakano and M. Murakami, "Velocity measurement of He II thermal counterflow jet accompanied by second sound Helmholtz oscillation," Cryogenics **34**, 179–185 (1994).
[22]A. Nakano, M. Murakami, and K. Kunisada, "Flow structure of thermal counterflow jet in He II," Cryogenics **34**, 991–995 (1994).

[23]J. H. W. Lee and V. H. Chu, *Turbulent Jets and Plumes* (Springer, 2003).
[24]C. G. Ball, H. Fellouah, and A. Pollard, "The flow field in turbulent round free jets," Prog. Aerosp. Sci. **50**, 1–26 (2012).
[25]M. Murakami, T. Takakoshi, M. Maeda, and A. Nakano, "PIV measurement result of superfluid He II thermal counterflow jet," AIP Conf. Proc. **985**, 183–190 (2008).
[26]P. Buchhave and C. M. Velte, "A similarity scaling model for the axisymmetric turbulent jet based on first principles," Phys. Fluids **34**, 095102 (2022).
[27]C. Zhu, Y. Tian, P. Buchhave, and C. M. Velte, "Similarity scaling of the axisymmetric turbulent jet," Phys. Fluids **34**, 095125 (2022).
[28]E. Varga, M. J. Jackson, D. Schmoranzer, and L. Skrbek, "The use of second sound in investigations of quantum turbulence in He II," J. Low Temp. Phys. **197**, 130–148 (2019).
[29]E. Woillez, J. Valentin, and P.-E. Roche, "Second sound resonators and tweezers as vorticity or velocity probes: Fabrication, model and method," arXiv:2301.05519 (2023).
[30]P. Švančara, "Experimental investigations of liquid helium flows," Ph.D. thesis (Charles University, Prague, Czech Republic, 2021).
[31]P.-E. Roche, P. Diribarne, T. Didelot, O. Français, L. Rousseau, and H. Willaime, "Vortex density spectrum of quantum turbulence," Europhys. Lett. **77**, 66002 (2007).
[32]E. Woillez, J. Valentin, and P.-E. Roche, "Local measurement of vortex statistics in quantum turbulence," Europhys. Lett. **134**, 46002 (2021).
[33]G. W. Stagg, N. G. Parker, and C. F. Barenghi, "Superfluid boundary layer," Phys. Rev. Lett. **118**, 135301 (2017).
[34]P. Švančara and M. La Mantia, "Coherent propagation of vortex rings at extremely high Reynolds numbers," J. Fluid Mech. **953**, A28 (2022).
[35]E. Varga, S. Babuin, and L. Skrbek, "Second-sound studies of coflow and counterflow of superfluid ^{4}He in channels," Phys. Fluids **27**, 065101 (2015).
[36]T. H. Weisgraber and D. Liepmann, "Turbulent structure during transition to self-similarity in a round jet," Exp. Fluids **24**, 210–224 (1998).
[37]H. J. Hussein, S. P. Capp, and W. K. George, "Velocity measurements in a high-Reynolds-number, momentum-conserving, axisymmetric, turbulent jet," J. Fluid Mech. **258**, 31–75 (1994).
[38]S. B. Pope, *Turbulent Flows* (Cambridge University Press, 2000).
[39]S. S. Aleyasin, M. F. Tachie, and M. Koupriyanov, "PIV measurements in the near and intermediate field regions of jets issuing from eight different nozzle geometries," Flow Turbul. Combust. **99**, 329–351 (2017).
[40]J. Salort, P.-E. Roche, and E. Lévêque, "Mesoscale equipartition of kinetic energy in quantum turbulence," Europhys. Lett. **94**, 24001 (2011).
[41]S. Babuin, E. Varga, L. Skrbek, E. Lévêque, and P.-E. Roche, "Effective viscosity in quantum turbulence: A steady-state approach," Europhys. Lett. **106**, 24006 (2014).
[42]R. A. Antonia, H. S. Shafi, and Y. Zhu, "A note on the vorticity spectrum," Phys. Fluids **8**, 2196–2202 (1996).
[43]O. Chanal, B. Chabaud, B. Castaing, and B. Hébral, "Intermittency in a turbulent low temperature gaseous helium jet," Eur. Phys. J. B **17**, 309–317 (2000).
[44]T. Ishihara, Y. Kaneda, M. Yokokawa, K. Itakura, and A. Uno, "Spectra of energy dissipation, enstrophy and pressure by high-resolution direct numerical simulations of turbulence in a periodic box," J. Phys. Soc. Jpn. **72**, 983–986 (2003).